ACS APPLIED NANO MATERIALS

www.acsanm.org Article

Up- and Down-Convertible LaF_3:Yb,Er Nanocrystals with a Broad Emission Window from 350 nm to 2.8 μm: Implications for Lighting Applications

Madhab Pokhrel,*,▽ Santosh K. Gupta,▽ Alan Perez, Brindaban Modak, Pampa Modak, Linda A. Lewis, and Yuanbing Mao*

Cite This: *ACS Appl. Nano Mater.* 2021, 4, 13562−13572 Read Online

ACCESS | Metrics & More | Article Recommendations | Supporting Information

ABSTRACT: In this study, emissions between 350 nm and 2.8 μm are produced from molten-salt-synthesized LaF_3:Yb^{3+},Er^{3+} (LFYE) nanocrystals (NCs) under 980 nm excitation. In fact, such wide spectral emissions from a single phosphor would be highly favorable in lighting applications ranging from light-emitting diodes, optical fibers, and telecommunications. Upconversion luminescence (UCL) spectra show intense red emission compared to the green band below 6 mW, wherein a strong green emission is achieved compared to a red emission when the laser power is increased beyond 85 mW. To further enhance their UCL and downconversion luminescence (DCL), the LFYE NCs are annealed at 400 °C for 30, 60, 90, and 120 min. Their UCL and DCL intensities are improved with up to 90 min of annealing but drastically reduced after annealing for 120 min. The latter is caused by both phase transition and shape changes, that is, from the cubic LFYE NCs to tetragonal LaOF:Yb^{3+},Er^{3+} (LOFYE) NCs with a square pyramidal shape. Density functional theory calculations show that the LOFYE NCs are more thermodynamically favorable to form due to their lower defect formation energy than the LFYE NCs. Moreover, LaF_3 is dynamically more unstable in comparison to LaOF, as indicated by a greater number of imaginary modes for LaF_3 in the phonon dispersion plot. Interestingly, the highest phonon energy for LaF_3 is found to be 439 cm^{-1} while that of LaOF is 527 cm^{-1}, which is expected to play a role in the different emission behaviors between LaF_3 and LaOF. Our work shows exemplary potential of the LFYE NCs with near-ultraviolet to mid-infrared emissions as UCL and DCL for laser power-induced color tunability for a wide range of applications.

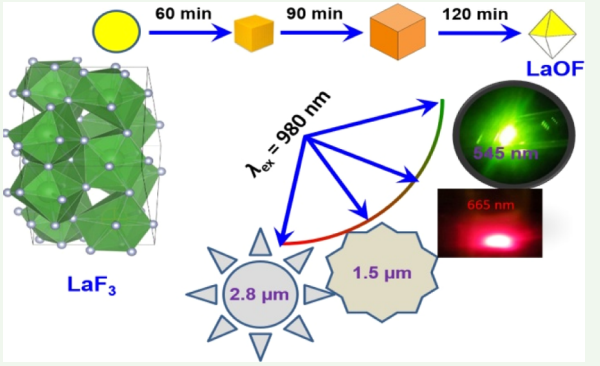

KEYWORDS: *LaF_3, LaOF, upconversion, downconversion, molten salt synthesis*

1. INTRODUCTION

Photon upconversion (UC) is a process of generating high-energy emission(s) from low-energy absorption via multiple photon absorption.[1] UC phosphors (UCPs) have found applications in four main aspects of modern days, that is, energy, security, health, and environment. UCPs are effective in improving the conversion efficiency in solar cells, bioimaging, and disinfecting bacteria present in water.[2−5] Near-infrared (NIR) excitation of UCPs is particularly useful for bioimaging owing to deep penetration depth, low or no autofluorescence, and reduced light scattering compared to ultraviolet (UV)/blue-green light excitation.[5] Generation of violet-blue photons from NIR light is also quite important for biomedical applications, photoinduced drug delivery, photodynamic therapy, and optogenetics where large anti-Stokes shift is needed.[6] On the other hand, efficient NIR and mid-infrared (MIR) emissions via downconversion (DC) are typically difficult to achieve but can be utilized in a wide variety of applications ranging from optical fiber communication, medical surgery, eye-safe laser radar, hazardous chemicals detection, remote sensing, pollution monitoring, and so forth.[6] Such wide light emission spanning the violet to MIR region would be a boon to the lighting community in designing efficient light-emitting diodes, solar panels, optical fibers, and a variety of other telecommunication-related applications.

Among rare-earth ions, erbium (Er^{3+}) is an important dopant for both UC and DC luminescence under one excitation wavelength due to its favorable energy level diagram. Along with UV and visible UC emissions, Er^{3+} shows multiple DC emissions in the NIR and MIR ranges, namely, $^4I_{13/2} \rightarrow {}^4I_{15/2}$ and $^4I_{11/2} \rightarrow {}^4I_{13/2}$ transitions. In terms of UC

Received: September 19, 2021
Accepted: November 19, 2021
Published: December 1, 2021

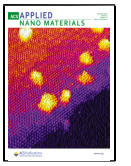

https://doi.org/10.1021/acsanm.1c03023
ACS Appl. Nano Mater. 2021, 4, 13562−13572

Scheme 1. MSS of the LaF_3 and LFYE NCs and the Effects of Annealing Duration on Their Shape and Crystal Structure

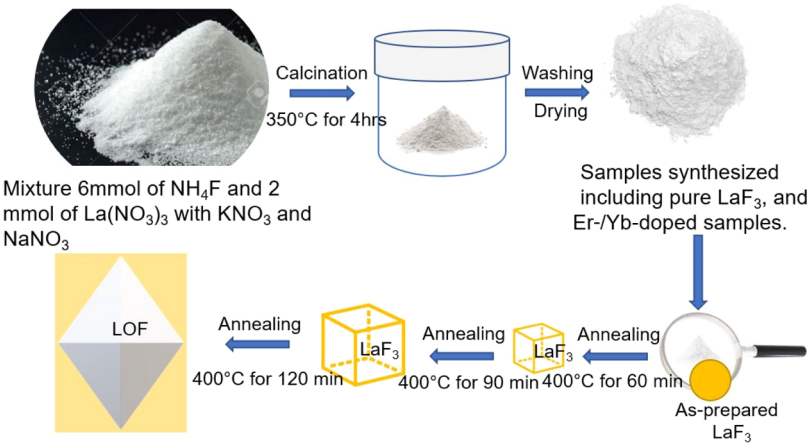

luminescence, Er^{3+} offers multiple radiative energy-level transitions in the visible range, including yellow-green $^2H_{11/2}$, $^4S_{3/2} \rightarrow {}^4I_{15/2}$, and red $^4F_{9/2} \rightarrow {}^4I_{15/2}$ transitions.[7,8] However, the forbidden nature of the Er^{3+} f−f transitions gives a low absorption coefficient, resulting in low UC and DC efficiencies.[9] Ytterbium (Yb), by contrast, has only a single energy transition of $^2F_{7/2} \rightarrow {}^2F_{5/2}$, which corresponds to 980 nm.[10] Due to an energy transition that coincides with the $^4I_{11/2} \rightarrow {}^4I_{15/2}$ transition of Er^{3+} and a large absorption cross-section (11.7×10^{-21} ions/cm^2), Yb is frequently used as a sensitizer that lends itself to highly productive UC and DC emission via energy transfer (ET). Especially, with the availability of cheaply available 980 nm laser diodes, there is an ample interest to improve the photon yield on both UC and DC emissions through Er channels on the Er-/Yb-doped host matrix by taking advantage of Yb → Er ET under 980 nm excitation.

Proper selection of host matrices has a strong influence on UC and DC efficiencies since the distance between lanthanide ions and their relative spatial location, local coordination number, and environment is determined by host lattices.[11] An ideal host matrix should be transparent in the spectral range of interest, possess a high optical damage threshold with low maximum phonon energy, and maintain chemical stability.[2,12] Lanthanum fluoride (LaF_3) is considered to be an excellent UC/DC host as it meets the above-mentioned criteria to endow both efficient NIR and MIR DC emissions and visible and UV UC emissions.[13] As reported, LaF_3 is optically transparent from the UV (250 nm, $n = 1.63$) to far infrared (up to 7 μm) range.[14,15] Based on its index of refraction value, that is, 1.4872 at 2.8 μm, LaF_3 is considered as an excellent host for MIR emission compared to that of visible UC. LaF_3:Yb^{3+},Er^{3+} (LFYE) as a three-component system has been explored extensively in the literature in the areas of UC and DC phosphors.[16−18] Er^{3+} and Yb^{3+} are used as dopants in the LaF_3 host to impart electronic transition levels and sensitization, respectively.

Moreover, UC and DC phosphors in the nanodomain have additional advantages of biocompatibility, water dispersibility, and cell uptake with negligible photobleaching. Thermal treatment has been used to enhance the UC and DC efficiencies of luminescent nanocrystals (NCs) due to increased crystallinity and reduced surface defects, heterogeneity, and deformities.[3,19] It leads to minimized nonradiative (multiphonon) relaxations for efficient photoluminescence (PL). Many researchers have exposed NCs to high-temperature annealing which promotes aggregate formation and potentially leads to light scattering. For LaF_3, some groups have also observed its phase transition to lanthanum oxyfluoride (LaOF).[18,20] For example, Zhang et al. reported the phase transition in LaF_3 when annealed at 500 °C just for 5 min.[18] To the best of our knowledge, no systematic studies on the optimal annealing duration and temperature for LaF_3 by avoiding its oxidation to LaOF and understanding the phase transition on the luminescence efficiencies have been reported.

In this work, we first synthesized LFYE NCs by a molten salt synthesis (MSS) method. The LFYE NCs showed multidimensional color emissions by upconverting 980 nm photons to visible light and downconverting it to NIR at ∼1550 nm and MIR at ∼2.8 μm. In addition, conversion of 980 nm light to near-UV (NUV)/violet-blue emissions was achieved, although the intensity was weaker than the green/red UC bands. We also investigated the effect of the Yb^{3+} sensitizer concentration on the UC and DC properties. Moreover, the red-to-green intensity ratio was completely tuned by adjusting the laser power beyond 6 mW.

To further optimize the UC and DC emissions of the as-synthesized LFYE NCs, we annealed them at a temperature as low as 400 °C with varying annealing durations between 30 and 120 min. The phase transition from LFYE to LaOF:Yb^{3+},Er^{3+} (LOFYE) was monitored using X-ray diffraction (XRD) and Raman spectroscopy. The UC and DC intensities of the LFYE NCs were further enhanced through systematic annealing to control multiphonon relaxation. The LFYE NCs had much higher UC and DC intensities compared to the LOFYE NCs, which were further probed using density functional theory (DFT) calculations. The negative formation energy and lower number of imaginary modes in the phonon dispersion plot indicated the higher stability of the LOFYE NCs compared to their LFYE counterpart.

Overall, the work detailed herein achieved violet-blue, green, red, NIR, and MIR emissions under 980 nm photon excitation from the LFYE NCs synthesized by the MSS method, followed by inducing phase transition to the LOFYE NCs upon annealing at 400 °C for 120 min or longer. At the same time, we demonstrated the laser power-induced tunable light emission. The effect of thermal treatment on UC intensity was also investigated in the preview of surface defects and structural changes. This concurrent UC and DC phosphor

https://doi.org/10.1021/acsanm.1c03023
ACS Appl. Nano Mater. 2021, 4, 13562−13572

holds great potentials to provide new ways in optical material design for multifunctional applications.

2. EXPERIMENTAL SECTION

To prepare pure LaF_3 NCs and derivatives doped with y mol % Yb^{3+} (y = 5, 7, 10, and 20) and 1.0 mol % Er^{3+}, a MSS method was used, as shown in Scheme 1.[21] The details of the methods and thermal annealing are given in Supporting Information S1 and S2, respectively. The obtained pure LaF_3 NCs were designated as LF. The LaF_3 NCs codoped with Yb^{3+} and Er^{3+} were designated as LFYE NCs in general while those doped with y mol % Yb^{3+} (y = 5, 7, 10, and 20) and 1.0 mol % Er^{3+} were denoted as LFY5E1, LY7E1, LY10E1, and LY20E1, respectively.

Also, the LF and LFYE NCs were thermally annealed in air at 400 °C for various time intervals, that is, 30, 60, 90, and 120 min. For simplicity, the annealed samples were denoted as "sample composition-annealing duration". For example, the LF NCs were named as "LF-60" after annealing at 400 °C for 60 min and the LFY7E1 NCs were named as "LFY7E1-30" after annealing at 400 °C for 30 min. In addition, the samples were also annealed at 450 and 500 °C for just 5 min (Supporting Information S3).

3. RESULTS AND DISCUSSION

3.1. Phase and Band Gap Analysis. XRD and Rietveld refinements of the LF samples before and after annealing at 400 °C for 90 min were conducted with the Fullprof software as an extension to the Match software (Supporting Information S4). The XRD pattern (Figure 1a) of the LF NCs synthesized by the MSS closely matches the standard pattern of LF with the hexagonal structure having the space group $P6_322$.[22] XRD patterns were also taken for the LFY5E1, LFY7E1, LFY10E1, and LFY20E1 NCs (Figure 1a). It can be clearly seen that the Er^{3+} and Yb^{3+} doping did not affect the XRD pattern of the LF NCs even with a high Yb^{3+} doping concentration. This suggested that the dopants were doped into the LF lattice without affecting the basic hexagonal structure even with a doping level as high as 21%.

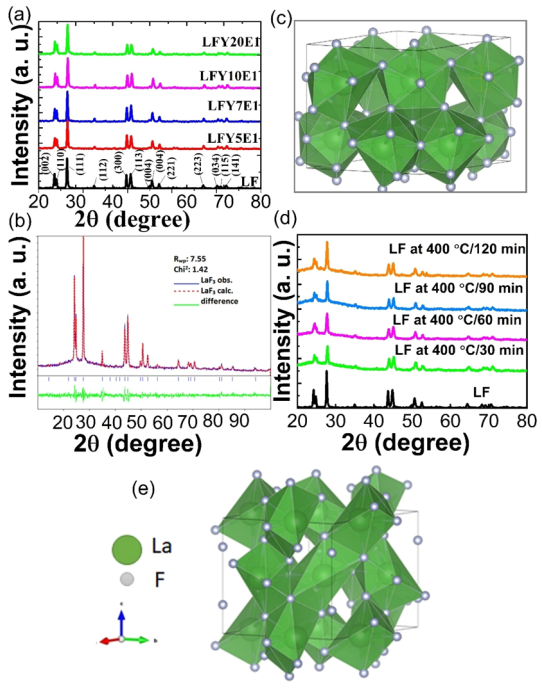

Figure 1. (a) XRD patterns of the LF, LFY5E1, LFY7E1, LFY10E1, and LFY20E1 NCs. (b) Experimental and Rietveld-refined XRD patterns of the LF NCs. (c) Rietveld-refined crystal structure of the LF NCs. (d) XRD patterns of the LF NCs before and after annealing at 400 °C for different annealing durations. (e) Rietveld-refined crystal structure of the LF NCs after annealing at 400 °C for 90 min.

To further evaluate the feasibility of the MSS method for the LF NCs, Rietveld refinement was first conducted on the XRD pattern of the LFNCs. The values of the weight Rietveld refinement (Figure 1b) parameter and goodness of fit (χ^2) were found to be 0.085 and 1.54%, respectively. The obtained lattice parameters from the refinement were found to be $a = b$ = 7.174 Å and c = 7.339 Å, which closely agreed with the previously reported values for LF possessing a similar structure and space group. The crystallite size and lattice strain were determined from the most intense peak (111) using the Debye Scherer's equation after subtracting the instrumental broadening determined from the monocrystalline silicon diffraction line and were found to be ∼38 nm and 0.55%, respectively.

The crystal structure (Figure 1c) of the LF NCs synthesized by the MSS method was drawn from the Rietveld-refined XRD data using the VESTA software, such as atomic coordinates, lattice parameters, and space group of $P6_322$. It was clearly inferred that the LF NCs assumed a hexagonal structure having three fluorine sublattices where the La^{3+} ions were located on the layers perpendicular to the c-axis.

No significant change in the XRD patterns of the LF NCs after annealing at 400 °C for different time intervals (i.e., 30, 60, 90, and 120 min) was noticed in terms of the peak broadening, position, or crystallite size (Figure 1d). This finding suggested that annealing did not change the original identity of the as-prepared LF NCs and held promise with an advantage of annealing for a longer time rather than annealing at a higher temperature.

Annealing at 400 °C for 90 min induced the structural transition from one hexagonal form of LF (SG-$P6_322$) to another with a different space group $P6_3cm$ (Figure 1e). The structural parameters of the LF NCs before and after annealing at 400 °C for 90 min are tabulated in Table 1. The annealing also led to a slight increase of the lattice parameter and cell volume. Upon further extending the annealing time to > 120 min and increasing annealing temperature > 400 °C, LOF was formed (Supporting Information S5 and Figure S1). Based on the stoichiometry of the LF structure under the excess F environment, we predicted that LOF adopted a tetragonal structure as it is also known to adopt a rhombohedral structure in some stoichiometry at room temperature.[22] As previously pointed out, the same samples showed a phase change of LF to LOF when annealed at 450 and 500 °C that occurs in just 5 min.

Table 1. Rietveld-Refined Structural Parameter of the LF NCs before and after Annealing at 400 °C for 90 min

LF NCs	before annealing	after annealing
crystal system	hexagonal	hexagonal
space group	$P6_322$ (182)	$P6_3cm$ (185)
lattice parameters (Å)	a = 7.14, c = 7.30	a = 7.15, c = 7.30
volume (Å^3)	322.59	323.02
R_{bragg}	7.55	9.99
R_f	10.4	13.8
χ^2	1.47	1.04

The band gap of the LF NCs was measured using the atomic positions from the Rietveld analysis and the HSE06 hybrid

https://doi.org/10.1021/acsanm.1c03023
ACS Appl. Nano Mater. 2021, 4, 13562−13572

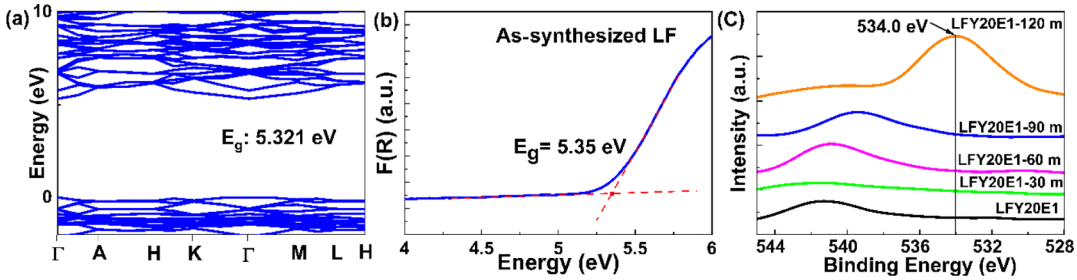

Figure 2. (a) DFT-calculated band structure and (b) Kubelka–Munk plot of the LF NCs. (c) O 1s XPS spectra of the LFY20E1 NCs before and after annealing at 400 °C for different intervals.

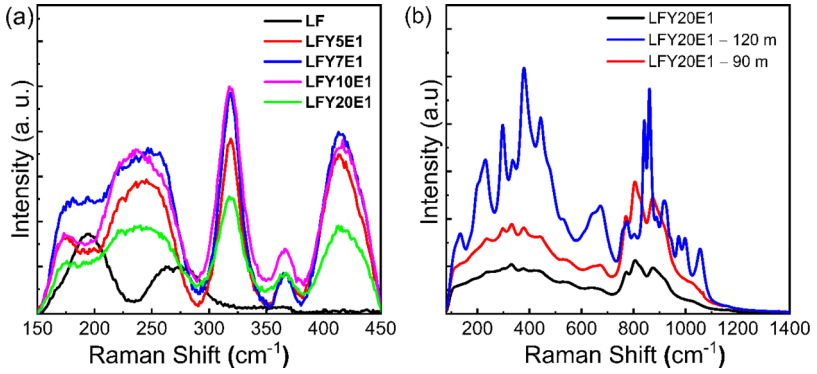

Figure 3. Raman spectra of the (a) LF, LFY5E1, LFY7E1, LFY10E1, and LFY20E1 NCs and (b) LFY20E1 NCs before and after annealing at 400 °C for 90 and 120 min.

functional (Figure 2a) and was found to be 5.32 eV, closely matching the experimentally determined band gap of 5.35 eV using diffuse reflection spectroscopy (Figure 2b) by employing Kubelka–Munk approximations and analogy. These results showed the high efficacy of the MSS for the synthesis of the LF NCs.

The phase transformation of the LF NCs to the LOF phase was also observed from O 1s X-ray photoelectron spectroscopy (XPS) spectra of the LFY20E1 NCs after annealing at 400 °C for 120 min (Figure 2c). The O 1s XPS spectral features remained similar after annealing up to 60 min, showing a peak around 541 eV corresponding to hydroxyl oxygen. However, when the annealing time was increased to 120 min, while the peak at 541 eV disappeared, a new peak around 534.5 eV evolved corresponding to the included oxygen atoms into the LF lattice.[23] The LFY20E1 NC samples annealed for shorter than 120 min showed only gradual binding energy (BE) shifts. This observation was manifested in the formation of the LOF lattice. The formation of LOF can also be manifested from the Raman spectra shown in Figure 3b.

3.2. Vibrational and Morphological Analysis. Single-crystal hexagonal LF with the point group D_{3d}^4 ($P\bar{3}C1$) has been reported to ideally consist of 17 Raman-active (5 A_{2u} + 12 E_u) modes, as elucidated based on the symmetry-adapted mode program available on the Bilbao crystallographic server.[24] In the case of the LF NCs (Figure 3a), fewer Raman-active modes were detected, which was expected unless polarization-dependent Raman measurements are conducted.[25] Interestingly, the LF NCs possessed only two Raman-active modes which were located at ~200 cm^{-1} (M1) and 275 cm^{-1} (M2). In the case of the LFYE NCs, three additional Raman-active modes at 325 cm^{-1} (M3), 360 cm^{-1} (M4), and 430 cm^{-1} (M5) were detected, while the M1 and M2 modes blue-shifted from 200 cm^{-1} → 175 cm^{-1} and 275 cm^{-1} → 240 cm^{-1}. According to the detailed experimental analysis and theoretical modeling of the Raman spectra of LF by Oreshonkov et al.,[26] the M1 and M5 Raman modes have an A_{1g} symmetry, whereas the M2, M3, and M4 modes have an E_g symmetry. The M1 mode at 200 cm^{-1} can be ascribed to F_2 ion translation along the *c*-axis, whereas the M2 band located at 275 cm^{-1} arises from the asymmetric stretching vibration of the La–F_1/F_2 bond. The appearance of the M3 band at 325 cm^{-1} from the LFYE NCs can be attributed to the asymmetric stretching vibration of the La–F_3 bond, that of the M4 band at 360 cm^{-1} to the F_1 ion translation along the *c*-axis, and that of the M5 band around 430 cm^{-1} from the mixed vibration of all three fluorine atoms together.

The transition from the LFNCs into the LOF phase was further confirmed by Raman spectroscopy (Figure 3b). For tetragonal LOF with a C_{4v} symmetry, six Raman-active modes were expected: A_{1g} + 2 B_{1g} + 3 E_g. All these six bands were detected from the LFY20E1 NCs in the range of 150–550 cm^{-1} once annealed at 400 °C for 120 min[27] The sharp and intense peak at 500 cm^{-1} was another unique signature of tetragonal LOF.[28] Moreover, La–O vibration modes appeared around 900 cm^{-1} from the LFY20E1 NCs once annealed at 400 °C for 120 min, which further indicated the oxidation of the LFY20E1 NCs into the LOF phase. Such phase transition could not be picked up by a lab XRD system with a Cu Kα source but could be sensed using a much more sensitive XPS system. Moreover, Raman spectroscopy being sensitive to metal–oxygen vibration can also identify the inclusion of lighter oxygen atoms.

To sum up, the XRD (Supporting Information S5), XPS, and Raman data confirmed the transition of the LF phase to LOF after annealing at 400 °C for 120 min. The typical LOF peaks in the XRD pattern were absent due to the weak ordering of the LOF structure and low resolving power of our

https://doi.org/10.1021/acsanm.1c03023
ACS Appl. Nano Mater. 2021, 4, 13562–13572

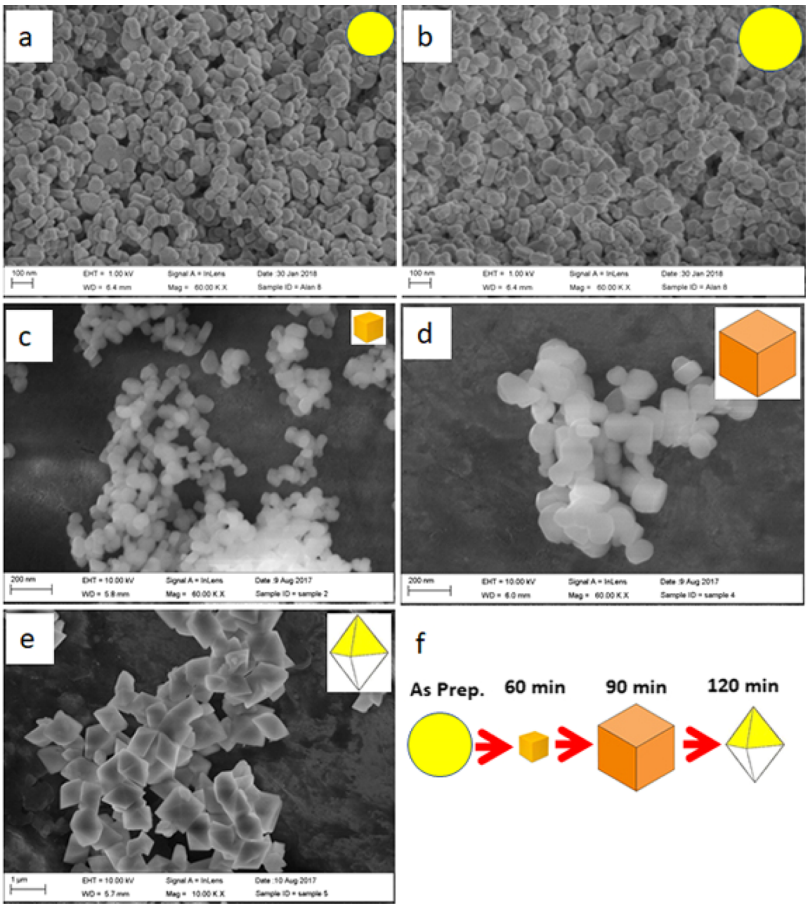

Figure 4. SEM images of the (a) LFY7E1 NCs, (b) LFY20E1 NCs, and LFY20E1 NCs after annealing at 400 °C for (c) 60, (d) 90, and (e) 120 min. (f) Schematic diagram showing the thermally induced shape transition of the LFY20E1 NCs from nanospheres to nanocubes and finally to square pyramids after annealing at 400 °C for different intervals.

diffractometer in addition to the possible broadening due to the high inclusion of oxygen in the LOF structure. However, as shown in Supporting Information S5 and XPS results, it was confirmed that our LF NCs slowly transitioned into a LOF structure with increasing annealing time and full transition once annealed at 400 °C for 120 min.

The representative SEM images of the LFY7E1 and LFY20E1 NCs (Figure 4a,b, respectively) clearly show the formation of NCs with a size of ∼50 nm. Thermal treatment of the LFYE NCs at 400 °C for different intervals not only induced transition from the hexagonal fluoride phase to the tetragonal oxyfluoride phase (Supporting Information S5) but also triggered shape change. As the LFY20E1 NCs were annealed at 400 °C for 60 min, the shape transformed from nanospheres (Figure 4a,b) to nanocubes (Figure 4c). Increasing the annealing time from 60 to 90 min led to an enhancement of the size of the nanocubes (Figure 4d). Once annealed at 400 °C for 120 min, a phase transition manifested in a shape change from nanocubes to square pyramids (Figure 4e,f). This observation could be explained through the nucleation rate of chemical species: longer annealing time induces more collisions among particles, while it leads to larger particles with more facets and corners, such as cubes and square pyramids.[29] If all the facets of LF grow at the same rate, it was reported that no phase transition would occur, but only the size of particles would change.[30] The fact that a progressive increase of the annealing time at the same annealing temperature led to a shape change from a sphere to cube to square pyramid suggested that some of the facets had lower interfacial energy and progressed with a lower growth rate compared to the other facets, while the specific mechanism needs further investigation in the future.[31]

3.3. UC and DC Luminescence of the LFYE NCs with Different Yb^{3+} Concentrations. The UC PL spectra of the LFYE NCs between 350 and 750 nm upon a 980 nm laser excitation (Figure 5a) depicted three major peaks located at ∼520, 545, and 665 nm, which can be attributed to the f−f transitions of Er^{3+} ions. The two adjoined peaks around 520 and 545 nm in the green spectral region are ascribed to the $^2H_{11/2} \rightarrow {}^4I_{15/2}$ and $^4S_{3/2} \rightarrow {}^4I_{15/2}$ transitions of the Er^{3+} ion. The most prominent red-emitting peak located at 665 nm is attributed to the $^4F_{9/2} \rightarrow {}^4I_{15/2}$ transition of Er^{3+}. No spectral profile change was observed as a function of the Yb^{3+} concentration, possibly owing to the absence of any Er^{3+}/Yb^{3+} clustering, which may lead to nonradiative decay of Er^{3+}-excited levels.[32] The integral emission intensity of the green and red peaks showed different variation trends with the Yb^{3+} doping level: the former maximized at 7 mol % (Figure 5b), whereas the latter exhibited a gradual increase without an indication of quenching up to the maximum doping level of 20 mol % performed in this study (Figure 5b). This suggests that an optimum sensitizer concentration (OSC) exists for Yb^{3+} to give maximum green and red UC emissions from the LFYE NCs. The OSC values were found to be 7 mol % for the green emission band and at 20 mol % or higher for the red band.

https://doi.org/10.1021/acsanm.1c03023
ACS Appl. Nano Mater. 2021, 4, 13562−13572

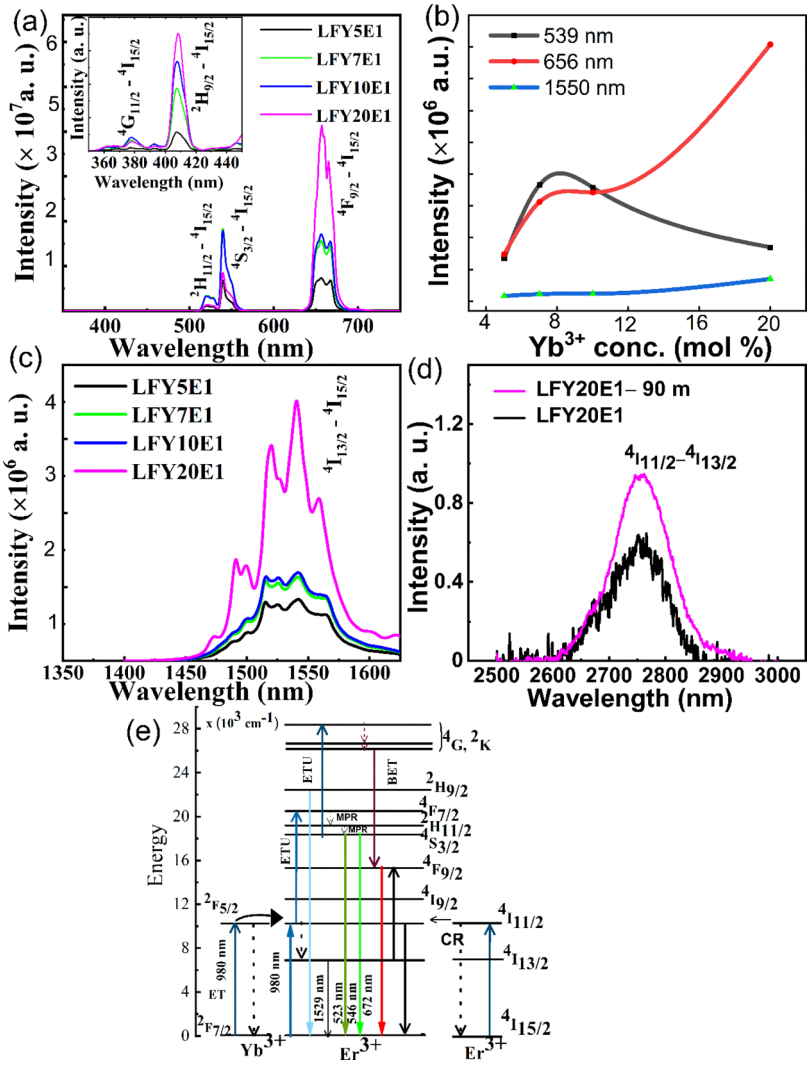

Figure 5. (a) UC visible emission spectra, (b) green and red UC, and the inset shows the DC NIR (1.55 μm) emission intensity variations as a function of the Yb^{3+} doping concentration, (c) DC NIR emission spectra at 1.55 μm from the LFY5E1, LFY7E1, LFY10E1, and LFY20E1 NCs under 980 nm excitation. (d) DC MIR (2.75 μm) emission spectra of the LFY20E1 NCs before and after annealing at 400 °C for 90 min and € energy level diagram of Er^{3+} and Yb^{3+} with the characteristic ET, ESA, and UC emissions of the LFYE NCs under 980 nm excitation. ETU, ESA, and MPR represent ET UC, ESA, and multiphonon relaxation, respectively.

This photophysical observation could be explained on the basis that the $^4I_{13/2} \rightarrow {}^4F_{9/2}$ electronic transition is effective at elevated Yb^{3+} concentrations.[33] Moreover, the cross-relaxation of $^4I_{7/2} \rightarrow {}^4F_{9/2}$ and $^4I_{13/2} \rightarrow {}^4F_{9/2}$ may enhance the red UC intensity.

The sensitizer concentration was restricted to an upper limit of 20 mol % as phase segregation is expected beyond 20 mol % Yb^{3+}. Higher Yb^{3+} ion concentrations induce quenching for green UC (Figure 5b) owing to the formation of Yb^{3+} clusters/aggregates, which are thought to lead to quenching through $Er^{3+} \rightarrow Yb^{3+}$ back-ET.[34] Hence, Yb^{3+} may act as trap states, resulting in radiationless relaxation at high doping levels instead of acting as a sensitizer.[35]

Moreover, the LFYE NCs also successfully converted the 980 nm photon to NUV light at ~360−380 nm and violet-blue light at ~400−420 nm (inset of Figure 5a). The NUV UC was attributed to $^4G_{11/2} \rightarrow {}^4I_{15/2}$ and the violet-blue UC was ascribed to $^2H_{9/2} \rightarrow {}^4I_{15/2}$ transitions of Er^{3+}. This involves an anti-Stokes shift of ~1.7 eV, which is equal to 2.954 eV (420 nm)—1.26 eV (980 nm) and, to the best of our knowledge, has never been reported.

Phosphors with NIR and MIR emissions within the second and third biological windows once excited by a 980 nm low-power constant-wave laser source have been considered as excellent optical probes for in vivo bioimaging.[36−41] Under 980 nm excitation, our LFYE NCs showed broad spectral features peaking around 1550 nm (NIR-B region) ascribed to the $^4I_{13/2} \rightarrow {}^4I_{15/2}$ transition of Er^{3+} (Figure 5c). This broad peak had several Stark components induced by the crystalline field of the LF lattice.[32] Spectral features were pronounced for this transition process, and the intensity at 1550 nm increased with the Yb^{3+} concentration (Figure 5b). The mechanism of the NIR emission at 1550 nm involves 980 nm excitation of Yb^{3+} from $^2F_{7/2}$ to $^2F_{5/2}$ states, followed by relaxation to the $^4I_{11/2}$ level of Er^{3+} via ET (Figure 5d). High-energy excitation states undergo nonradiative relaxation to the $^4I_{13/2}$ level of Er^{3+}, followed by emission at ~1550 nm owing to an $^4I_{13/2} \rightarrow {}^4I_{15/2}$ electronic transition (Figure 5d).[42] Moreover, the DC emission intensity increased monotonically with increasing

https://doi.org/10.1021/acsanm.1c03023
ACS Appl. Nano Mater. 2021, 4, 13562−13572

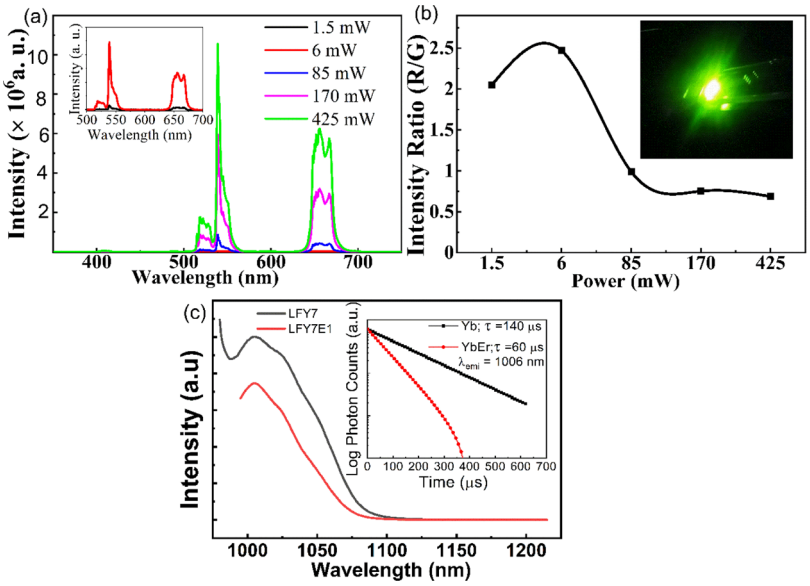

Figure 6. (a) UC emission spectra at different laser powers for LFY7E1 NCs under 980 nm excitation. The inset shows the enlarged version of the UC emission spectra at 1.5 and 6 mW and (b) variation of the red/green light intensity ratio as a function of the laser power. The inset in Figure 5b represents an acquired digital image under the laser power of 425 mW, depicting extremely bright green color. (c) Emission spectra of Yb^{3+} ions in the singly doped LFY7 NCs and the Er^{3+}/Yb^{3+} codoped LFY7E1 NCs. The inset shows the decay profiles of the emission at 1006 nm from both the samples.

Yb^{3+} concentration (Figure 5b), analogous to the red band in the case of the UC process.

Additionally, MIR emission was observed around 2.8 μm (Figure 5d) from the LFYE NCs as a result of the $^4I_{11/2} \rightarrow {}^4I_{13/2}$ electronic transition of Er^{3+}, as proposed in the energy level diagram shown in Figure 5e. The electrons in the ground state excited to $^4I_{11/2}$ through ground-state absorption under 980 nm excitation and decayed by radiative relaxation to the $^4I_{13/2}$, producing the emission at 2.8 μm, as represented by the LFY20E1 NCs (Figure 5d). Moreover, the intensity of this peak was relatively low.

The energy level diagram of Er^{3+} and Yb^{3+} ions depicted in Figure 5e illustrates the existing UC phenomena of the LFYE NCs. The property was largely facilitated by the $Yb^{3+} \rightarrow Er^{3+}$ ET owing to the efficient absorption of the 980 nm photon by the Yb^{3+} ion having a large NIR absorption cross section. Upon absorbing 980 nm NIR light, an Yb^{3+} electron moves to the $^2F_{5/2}$ excited level and then relaxes to $^4I_{11/2}$ of Er^{3+} via UC ET due to the closely matching energy of these two states. Subsequently, the second photon absorption leads to the excitation of Er^{3+} ions from $^4I_{11/2} \rightarrow {}^4F_{7/2}$, followed by nonradiative relaxation to lower energy states. These processes result in the emissions of green/red light at 520, 545, and 665 nm from the $^2H_{11/2}$, $^4S_{3/2}$, and $^4F_{9/2}$ states, respectively. Moreover, the red emission can appear through two different processes. The first one is through the UC ET of the $^4S_{3/2} \rightarrow {}^4F_{9/2}$ transition, as mentioned above. The other one involves populating the $^4I_{13/2}$ level via nonradiative transitions of $^4I_{11/2} \rightarrow {}^4I_{13/2}$ and then the latter excited to the $^4F_{9/2}$ level either through an ET process (Figure 5d) as $^2F_{5/2}$ (Yb^{3+}) + $^4I_{13/2}$ (Er^{3+}) $\rightarrow$ $^2F_{7/2}$ (Yb^{3+}) + $^4F_{9/2}$ (Er^{3+}) or an excited-state absorption (ESA) process as photon + $^4I_{13/2}$ (Er^{3+}) $\rightarrow$ $^4I_{15/2}$ (Er^{3+}) + $^4F_{9/2}$ (Er^{3+}).[43]

3.4. Tuning the UC Luminescence of the LFYE NCs through Laser Power. Interestingly, the UC intensity was found to be tunable through laser power. For example, for the LFY7E1 NCs, when the laser power was below 6 mW, the integrated red emission intensity was much higher than the green one (Figure 6a). However, the intensity ratio was reversed when the laser power increased above 85 mW with a predominant green emission. In fact, for the entire laser power range of 85−425 mW, the green emission intensity was higher than the red one.

Referring to the R/G ratio plot (Figure 6b) and power law analysis (Figure S3), the relationship of $n_{red} > n_{green}$ indicates that the green emission was produced due to a two-photon process, whereas the red emission was produced via a three-photon process. Although the mechanism for the three-photon process causing red emission is not firmly established, the dependence of the R/G ratio on excitation power (Figure 6a) ensured that a three-photon process was active for the red UC emission. Furthermore, MPR (Figure 5e) shows that the R/G ratio was constant if the green emission level contributed significantly to the red UC. On the other hand, the red and blue UC emissions under the same excitation at 980 nm support the proposed mechanism of the three-photon process, that is, the red and blue UC emissions were primarily generated by the three-photon process. This clearly indicates the involvement of manifolds of states ($^4G/^2K$), as shown in Figure 5e above the blue emission state of $^2H_{9/2}$. The competing radiative and nonradiative decays from $^4G/^2K$ states determine the relative intensity of the red and blue UC emission intensity. This mechanism is consistent with pump power dependence of the red UC emission, which suggests that a three-photon process is involved in the red and blue emissions. Shao et al. also observed color-tunable UC by varying the laser power.[44] Chen et al. obtained a ∼6-fold increase in the red-to-green emission tunability (from 0.19 to 0.49) by increasing the excitation power from 1.25 to 46.25 W·cm^{-2}.[45] In another report, raising the laser power from 1.6 × 10^4 to 2.5 × 10^6 W·cm^{-2} enhanced the UC intensity of $NaYF_4$:Yb^{3+},Tm^{3+} significantly.[4] Such pump power-dependent color tunability is ascribed to different excitation rates for

https://doi.org/10.1021/acsanm.1c03023
ACS Appl. Nano Mater. 2021, 4, 13562−13572

populating the $^4S_{3/2}$ and $^4F_{9/2}$ states.[46] Since the red and green emissions are governed by different power laws ($n_{red} > n_{green}$), it is expected that the $^4S_{3/2}$ state is more populated compared to the $^4F_{9/2}$ states at a high laser power (> 85 mW), thus enhancing the green emission over the red emission. This overlaps with the widely accepted process that three photons are involved in red emission where only two photons are involved for green emission, similar to what was reported for $NaYF_4/Yb^{3+},Er^{3+}$.[47]

The power dependence of the green emission intensity alone indicates the possibility of both red and green UC emissions also happening via the same three-photon process with the MPR relaxation pathway from Er^{3+} ($^4G/^2K$). However, we ruled out this pathway to populate the green emission level ($^4S_{3/2}$) since the R/G emission intensity ratio was not consistent with the pump power.

Figure 6c shows the emissions from the Yb^{3+} ion in the singly doped LFY7 NCs and the Yb^{3+}/Er^{3+} codoped LFY7E1 NCs. The decrease in the emission intensity in the codoped sample clearly indicates the ET from Yb^{3+} to Er^{3+}. From the measured decay times at 1006 nm in the singly doped LFY7 NCs and the codoped LFY7E1 NCs, the ET efficiency can be calculated using the equation

$$\eta = 1 - \frac{\tau}{\tau_0}$$

where τ is the decay time of Yb^{3+} ions in the presence of Er^{3+} ions and τ_0 is the decay time of Yb^{3+} ions without codoped Er^{3+} ions. The ET efficiency, also known as the internal quantum yield of the LFY7E1 NCs, was found to be 57%. This shows that nonradiative processes such as multiphoton relaxation, vibrational losses from other functional groups, and donor−acceptor interactions quench the UC luminescence (UCL) intensity and ET efficiency. The low UC efficiency of the LFY7E1 NCs also offered us the possibility of increasing the DC emission intensity at 1550 nm and 2.8 μm by optimizing the dopant concentration. The increase of the emission intensity at 1550 nm from the LFY10E1 and LFY20E1 samples with high Yb concentration as shown in Figure 5c proves that DC emissions in the LF host can be optimized with the right dopant concentration. Additionally, we succeeded in collecting emission at 2.8 μm from the LFY20E1 powder sample (Figure 5d). This analysis concludes that low UC ET efficiency offers the possibility of increasing the infrared quantum yield by optimizing the dopant concentration.

4. EFFECT OF THERMAL TREATMENT

The UC and DC emissions of the as-synthesized LFYE NCs may be enhanced by annealing owing to lowering surface defect-related quenching. Surface defects are known to provide additional nonradiative paths and hold a potential to severely affect the emission intensity of luminescent NCs. We investigated the effects of both annealing temperatures of 400 and 450 °C for 5, 30, 60, 90, and 120 min in the air to aid in identifying the point at which oxidation occurs. Once annealed at 400 °C for 120 min or at 450 °C for all treatment times, the LFYE NCs showed weakened luminescence emission (Supporting Information S6 and S2), so we only focused our study on the NCs annealed at 400 °C up to 120 min for further evaluations in this study.

The UC and DC PL emissions of the LFY20E1 NCs before and after annealing at 400 °C for different durations were compared in Figure 7a,b. For both UC (Figure 7a) and DC PL (Figure 7b), progressive increases in the emission intensity

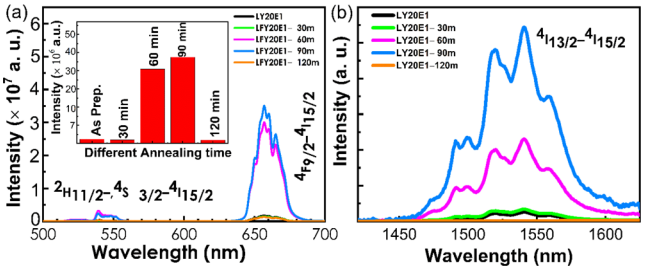

Figure 7. (a) Red and green UC PL spectra of the LFY20E1 NCs before and after annealing at 400 °C for different durations. The inset shows the UC PL intensity at 656 nm vs annealing time. (b) DC PL spectra at 1.55 μm of the LFY20E1 NCs before and after annealing at 400 °C for different durations.

were obtained up to 90 min, followed by detrimental decreases at longer annealing times. The initial rise of the UC and DC emission intensity can be ascribed to the improved crystallinity and decreased surface defects, which provide nonradiative pathways for relaxation. The detrimental decreases of the UC and DC emission intensities for the LFY20E1 NCs after annealing at 400 °C for 120 min were due to the inclusion of lighter oxygen atoms in LaF_3 into LaOF, accompanied by the enhanced extent of nonradiative vibrational relaxation and raised phonon energy.

The higher phonon frequency of LOF based on the phonon frequency calculations discussed later further confirms this analogy. Moreover, compared to the nanospheres/nanocubes which are more uniform in shape, square pyramids may cause scattering of both excitation and emitted photons with lowered PL intensity.

5. THEORETICAL CALCULATIONS

5.1. Crystal Structures of LF and LOF. In the present work, the symmetry space group of LF was considered as $P6_3cm$ (space group no. 185).[48] The crystal structure of LF contains six formula units per unit cell (see Supporting Information S7), which has four nonequivalent fluorine sites in the ratio of 6:6:4:2 (Figure 8a). With the PBE functional, the calculated optimized lattice parameters of LF were $a = b = 7.27$ Å and $c = 7.42$ Å (cell volume = 679.34 Å^3), which were in good agreement with the experimental values after Rietveld refinement of the XRD data (Figure 1b). The La−F bond lengths varied as 2.43, 2.46, 2.48, 2.50, and 2.55 Å, which were in good agreement with the earlier reported value.[49] This indicated that our calculation methodologies were realistic and the results should be reliable.

On the other hand, for LOF, we considered the crystal structure as a tetragonal with the space group $P4/nmm$ (129), where La ions were bonded in a body-centered cubic geometry to four O atoms and four F atoms (Figure 8b). The calculated lattice parameters for the optimized geometry of LOF were found to be $a = b = 4.113$ Å and $c = 5.881$ Å, which were consistent with the earlier reported values of $a = b = 4.092$ Å and $c = 5.857$ Å.[50] The calculated La−O and La−F bond lengths in the optimized geometry of LOF were found to be 2.65 and 2.41 Å, respectively.

To model the LFYE and LOFYE, we considered a 48-atom supercell and replaced two La atoms with Yb and Er (see

https://doi.org/10.1021/acsanm.1c03023
ACS Appl. Nano Mater. 2021, 4, 13562−13572

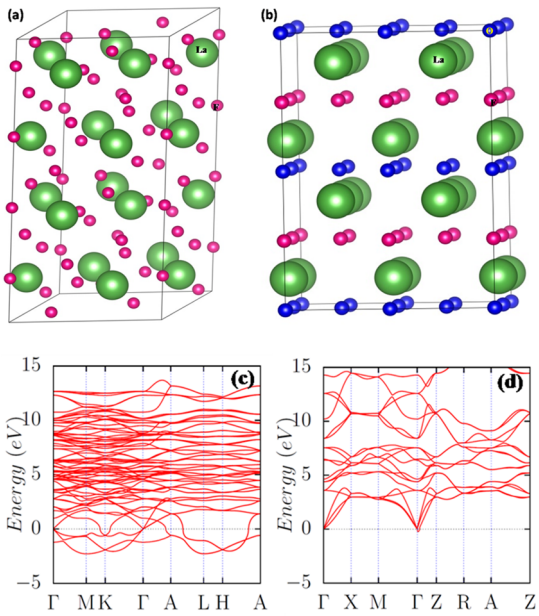

Figure 8. Crystal structures of (a) LF (1 × 1 × 2 supercell) and (b) LOF (2 × 2 × 2 supercell). Green, pink, and blue spheres represent La, F, and O atoms, respectively. Phonon dispersion plots of (c) LF and (d) LOF.

Supporting Information S7). In both cases, we considered different geometries by varying the relative distances between the dopant elements. For example, in one case, the chosen La sites were in the first nearest neighboring lattice sites of each other, which we designated as the "near" configuration. For the second case, the chosen La sites were in the third nearest neighboring lattice sites of each other, which we designated as the "far" configuration. All the structures were optimized by fully relaxing both cell parameters and ionic positions. Both types of configurations were energetically close to each other for both LFYE and LOFYE. Interestingly, for LFYE, the "near" configuration was energetically more stable than the "far" configuration, while for LOFYE, the reverse trend was observed. DFT clearly suggests the feasibility to stabilize both the LFYE and LOFYE NCs under different conditions with different geometrical orientations. Experimentally, we observed that different thermal conditions only led to a phase transition from LF to LOF.

5.2. Defect Formation Energies of LFYE and LOFYE. To find out the relative stability of the LFYE and LOFYE NCs, their defect formation energies were calculated. The defect formation energies of different configurations were computed using the relationship below[51]

$$\Delta H_f = E_{doped} - E_{perfect} + q\sum n_x \mu_x \quad (1)$$

where E_{doped} and $E_{perfect}$ represent the energies of the doped and perfect LF and LOF systems, calculated with the same supercell size, μ_x indicates the chemical potential of the element X, and n_x is the number of elements added ($q = -1$) or replaced ($q = +1$) to form defect systems. The calculation of defect formation energy indicated that the geometry with the dopant elements occupying the nearest neighboring lattice sites was more stable in LF, whereas the geometry with the dopant elements far away from each other was more stable in LOF. The calculated defect formation energies for the LFYE system with "near" and "far" configurations were 0.28 and 0.35 eV, respectively. It is interesting to note that the calculated defect formation energies for the LOFYE system with "near" and "far" configurations were negative with values of −0.11 and −0.14 eV, respectively. Thus, the formation of the LOFYE system was more thermodynamically favorable than that of the LFYE system. Thus, DFT data supported the fact that the LFYE to LOFYE transition was thermodynamically feasible as we observed experimentally.

5.3. Phonon Calculation of LF and LOF. We also calculated the phonon frequencies using and the phonon dispersion along the high-symmetry K-path of the Brillouin zone of both LF and LOF using the DFT and PBE methods, respectively.[7] The phonon dispersion plots (Supporting Information S7, Figure 8c,d) calculated using the PBE method showed a greater number of imaginary modes for LF than LOF. This indicated that LF was dynamically more unstable than LOF. Interestingly, the highest phonon energy of LF was found to be 439 cm^{-1}, while that of LOF was 527 cm^{-1}. The higher phonon energy of LOF was attributed to the presence of oxygen. We believe that this aspect had a significant role in the higher UC and DC efficiencies of the LFYENCs compared to the LOFYE NCs, as demonstrated in Figure 7.

6. CONCLUSIONS

In summary, LFYE NCs with different Yb^{3+} concentrations (5, 17, 10, and 20%) with a fixed 1 mol % of Er were produced using MSS. The LFYE NCs showed broad UC and DC emissions covering 270 nm−2.8 μm. The LFYE NCs demonstrated unusual UC bands in violet and blue colors with an anti-Stokes shift of more than 1 eV, which was rarely observed in earlier work. The LFYE NCs also showed intense DC emission at ∼1550 nm (NIR) and 2800 nm (MIR), which also progressively showed enhanced emission up to 20 mol % Yb^{3+}. Green-red visible UC interestingly showed laser power-tunable color emission wherein at a laser power lower than 6 mW, the red emission intensity was very high compared to the green intensity, but green emission predominated at high laser power. Such a wide emission window from a single phosphor which can also be tuned using laser power would be highly beneficial to the lighting community in designing tunable phosphors, light-emitting diodes, optical fibers, and in the area of telecommunications. Furthermore, thermal treatment at different durations at 400 °C led to shape (sphere → cube → square pyramids) and phase changes, whose implications on UC intensity were visible. Also, a phase transition from hexagonal LF to tetragonal LOF was observed after annealing at 400 °C for 120 min. DFT calculations pinpointed the fact that the LFYE to LOFYE conversion was thermodynamically feasible. Moreover, UC intensity quenched dramatically in the LaOF phase, which was validated and supported by the DFT-calculated phonon energy owing to the inclusion of lighter oxygen which facilitates nonradiative transitions. This work showed an exemplary potential of the molten salt-synthesized LFYE NCs to produce a wide range of emission profiles from NUV to MIR, considering laser power-induced color tunability and thermal annealing time variation to induce shape and phase change with implications on UCL and DCL.

■ ASSOCIATED CONTENT

Supporting Information

The Supporting Information is available free of charge at https://pubs.acs.org/doi/10.1021/acsanm.1c03023.

https://doi.org/10.1021/acsanm.1c03023
ACS Appl. Nano Mater. 2021, 4, 13562−13572

Information related to materials, MSS, thermal annealing, instrumentation, theoretical methodology, XRD patterns, UC luminescence comparison, and UC intensity vs excitation power double logarithmic plot (PDF)

AUTHOR INFORMATION

Corresponding Authors

Madhab Pokhrel − *Department of Physics and Astronomy, University of Texas Rio Grande Valley, Edinburg, Texas 78539, United States*; Email: madhab.pokhrel@utrgv.edu

Yuanbing Mao − *Department of Chemistry, Illinois Institute of Technology, Chicago, Illinois 60616, United States*; orcid.org/0000-0003-2665-6676; Email: ymao17@iit.edu

Authors

Santosh K. Gupta − *Radiochemistry Division, Bhabha Atomic Research Centre, Mumbai 400085, India; Homi Bhabha National Institute, Mumbai 400094, India*; orcid.org/0000-0002-1178-0159

Alan Perez − *Department of Physics and Astronomy, University of Texas Rio Grande Valley, Edinburg, Texas 78539, United States*

Brindaban Modak − *Chemistry Division, Bhabha Atomic Research Centre, Mumbai 400085, India; Homi Bhabha National Institute, Mumbai 400094, India*

Pampa Modak − *Radiological Safety Division, Atomic Energy Regulatory Board, Mumbai 400094, India; Homi Bhabha National Institute, Mumbai 400094, India*

Linda A. Lewis − *Chemical Sciences Division, Oak Ridge National Laboratory, Oak Ridge, Tennessee 37830, United States*

Complete contact information is available at: https://pubs.acs.org/10.1021/acsanm.1c03023

Author Contributions

$^{\nabla}$MP and SKG contributed equally.

Notes

The authors declare no competing financial interest.

ACKNOWLEDGMENTS

AP and MP would like to acknowledge the research grant from the Oak Ridge National Laboratory. MP would also like to acknowledge the financial support by the NSF under NSF CREST Center for Multidisciplinary Research Excellence in Cyber-Physical Infrastructure Systems (award #2112650). YM would like to thank the financial support by the NSF under CHE (award #1952803) and the IIT start-up funds. SKG thanks the United States−India Education Foundation (USIEF) and the Institute of International Education (IIE) for the Fulbright Nehru Postdoctoral Fellowship (award #2268/FNPDR/2017).

REFERENCES

(1) Bian, W.; Zhou, M.; Chen, G.; Yu, X.; Pokhrel, M.; Mao, Y.; Luo, H. Upconversion luminescence of ytterbium and erbium co-doped gadolinium oxysulfate hollow nanoparticles. *Appl. Mater. Today* **2018**, *13*, 381−386.

(2) Ryszczyńska, S.; Trejgis, K.; Marciniak, Ł.; Grzyb, T. Upconverting SrF_2:Er^{3+} Nanoparticles for Optical Temperature Sensors. *ACS Appl. Nano Mater.* **2021**, *4*, 10438.

(3) Srivastava, B. B.; Gupta, S. K.; Mao, Y. Single red emission from upconverting $ZnGa_2O_4$:Yb,Er nanoparticles co-doped by Cr^{3+}. *J. Mater. Chem. C* **2020**, *8*, 6370−6379.

(4) Zhao, J.; Jin, D.; Schartner, E. P.; Lu, Y.; Liu, Y.; Zvyagin, A. V.; Zhang, L.; Dawes, J. M.; Xi, P.; Piper, J. A.; Goldys, E. M.; Monro, T. M. Single-nanocrystal sensitivity achieved by enhanced upconversion luminescence. *Nat. Nanotechnol.* **2013**, *8*, 729−734.

(5) Zhou, L.; Wang, R.; Yao, C.; Li, X.; Wang, C.; Zhang, X.; Xu, C.; Zeng, A.; Zhao, D.; Zhang, F. Single-band upconversion nanoprobes for multiplexed simultaneous in situ molecular mapping of cancer biomarkers. *Nat. Commun.* **2015**, *6*, 1−12.

(6) Zhang, Z.; Xu, C.; Huang, B.; Wang, Y.; Pei, J.; Zheng, C.; Sun, L. Increasing ZnF_2 content enhancing the near- and mid-infrared emission in Er^{3+}/Yb^{3+} codoped oxyfluorotellurite glasses with decreased hydroxyl. *J. Lumin.* **2019**, *216*, 116683.

(7) Gupta, S. K.; Garcia, M. A. P.; Zuniga, J. P.; Abdou, M.; Mao, Y. Visible and ultraviolet upconversion and near infrared down-conversion luminescence from lanthanide doped $La_2Zr_2O_7$ nanoparticles. *J. Lumin.* **2019**, *214*, 116591.

(8) Pokhrel, M.; Kumar, G. A.; Sardar, D. K. Highly efficient NIR to NIR and VIS upconversion in Er^{3+} and Yb^{3+} doped in M_2O_2S (M = Gd, La, Y). *J. Mater. Chem. A* **2013**, *1*, 11595−11606.

(9) Gupta, S. K.; Abdou, M.; Zuniga, J. P.; Ghosh, P. S.; Mao, Y. Li^+ co-doping induced phase transition as an efficient strategy to enhance upconversion of $La_2Zr_2O_7$:Er,Yb nanoparticles. *J. Lumin.* **2020**, *224*, 117312.

(10) Kumar, G. A.; Pokhrel, M.; Sardar, D. K. Absolute quantum yield measurements in Yb/Ho doped M_2O_2S (M=Y, Gd, La) upconversion phosphor. *Mater. Lett.* **2013**, *98*, 63−66.

(11) Chen, C.; Li, C.; Shi, Z. Current Advances in Lanthanide-Doped Upconversion Nanostructures for Detection and Bioapplication. *Adv. Sci.* **2016**, *3*, 1600029.

(12) Naccache, R.; Yu, Q.; Capobianco, J. A. The Fluoride Host: Nucleation, Growth, and Upconversion of Lanthanide-Doped Nanoparticles. *Adv. Opt. Mater.* **2015**, *3*, 482−509.

(13) Xu, Y.; Zhang, X.; Dai, S.; Fan, B.; Ma, H.; Adam, J.-l.; Ren, J.; Chen, G. Efficient Near-Infrared Down-Conversion in Pr^{3+}−Yb^{3+} Codoped Glasses and Glass Ceramics Containing LaF_3 Nanocrystals. *J. Phys. Chem. C* **2011**, *115*, 13056−13062.

(14) Amotchkina, T.; Trubetskov, M.; Hahner, D.; Pervak, V. Characterization of e-beam evaporated Ge, YbF_3, ZnS, and LaF_3 thin films for laser-oriented coatings. *Appl. Opt.* **2020**, *59*, A40−A47.

(15) Marcos, L. V. R.-d.; Larruquert, J. I.; Méndez, J. A.; Aznárez, J. A. Self-consistent optical constants of MgF_2, LaF_3, and CeF_3 films. *Opt. Mater. Express* **2017**, *7*, 989−1006.

(16) Poma, P. Y.; Sales, T. O.; Kumar, K. U.; Jacinto, C. Role of heat treatment on the structural and luminescence properties of Yb^{3+}/Ln^{3+} (Ln = Tm, Ho and Er) co-doped LaF_3 nanoparticles. *Phys. Chem. Chem. Phys.* **2020**, *22*, 24535−24543.

(17) Secu, C. E.; Matei, E.; Negrila, C.; Secu, M. The influence of the nanocrystals size and surface on the Yb/Er doped LaF_3 luminescence properties. *J. Alloys Compd.* **2019**, *791*, 1098−1104.

(18) Zhang, H.; Dong, X.; Jiang, L.; Yang, Y.; Cheng, X.; Zhao, H. Comparative analysis of upconversion emission of LaF_3:Er/Yb and LaOF:Er/Yb for temperature sensing. *J. Mol. Struct.* **2020**, *1206*, 127665.

(19) Fu, L.; Wang, J.; Chen, N.; Ma, Q.; Lu, D.; Yuan, Q. Enhancement of long-lived luminescence in nanophosphors by surface defect passivation. *Chem. Commun.* **2020**, *56*, 6660−6663.

(20) Zhu, B.; Chen, N.; Zhu, D.; Li, Y.; Sun, W.; Liu, G.; Du, G. Thermal annealing of LaF_3:Eu^{3+} nanocrystals synthesized by a solvothermal method and their luminescence properties. *J. Sol-Gel Sci. Technol.* **2013**, *66*, 126−132.

(21) Gupta, S. K.; Mao, Y. Recent Developments on Molten Salt Synthesis of Inorganic Nanomaterials: A Review. *J. Phys. Chem. C* **2021**, *125*, 6508−6533.

(22) Jacob, K. T.; Saji, V. S.; Waseda, Y. Lanthanum Oxyfluoride: Structure, Stability, and Ionic Conductivity. *Int. J. Appl. Ceram. Technol.* **2006**, *3*, 312−321.

(23) Gupta, S. K.; Sahu, M.; Ghosh, P. S.; Tyagi, D.; Saxena, M. K.; Kadam, R. M. Energy transfer dynamics and luminescence properties of Eu^{3+} in $CaMoO_4$ and $SrMoO_4$. *Dalton Trans.* **2015**, *44*, 18957−18969.
(24) Kroumova, E.; Aroyo, M.; Perez-Mato, J.; Kirov, A.; Capillas, C.; Ivantchev, S.; Wondratschek, H. Bilbao crystallographic server: useful databases and tools for phase-transition studies. *Phase Transitions A Multinatl. J.* **2003**, *76*, 155−170.
(25) Patro, L. N.; Bharathi, K. K.; Raju, N. R. C. Microstructural and ionic transport studies of hydrothermally synthesized lanthanum fluoride nanoparticles. *AIP Adv.* **2014**, *4*, 127139.
(26) Oreshonkov, A. S.; Roginskii, E. M.; Krylov, A. S.; Ershov, A. A.; Voronov, V. N. Structural, electronic and vibrational properties of LaF_3 according to density functional theory and Raman spectroscopy. *J. Phys.: Condens. Matter* **2018**, *30*, 255901.
(27) Hölsä, J.; Piriou, B.; Räsänen, M. IR-and Raman-active normal vibrations of rare earth oxyfluorides, REOF; RE = Y, La, and Gd. *Spectrochim. Acta Part A Mol. Spectrosc.* **1993**, *49*, 465−470.
(28) Rodrigues, E. M.; Souza, E. R.; Monteiro, J. H. S. K.; Gaspar, R. D. L.; Mazali, I. O.; Sigoli, F. A. Non-stabilized europium-doped lanthanum oxyfluoride and fluoride nanoparticles well dispersed in thin silica films. *J. Mater. Chem.* **2012**, *22*, 24109−24123.
(29) Torres-Gómez, N.; Nava, O.; Argueta-Figueroa, L.; García-Contreras, R.; Baeza-Barrera, A.; Vilchis-Nestor, A. R. Shape tuning of magnetite nanoparticles obtained by hydrothermal synthesis: effect of temperature. *J. Nanomater.* **2019**, *2019*, 7921273.
(30) Sau, T. K.; Rogach, A. L. Nonspherical noble metal nanoparticles: colloid-chemical synthesis and morphology control. *Adv. Mater.* **2010**, *22*, 1781−1804.
(31) Ghosh, S.; Manna, L. The Many "Facets" of Halide Ions in the Chemistry of Colloidal Inorganic Nanocrystals. *Chem. Rev.* **2018**, *118*, 7804−7864.
(32) Perrella, R. V.; Ribeiro, I. C.; Campos-Junior, P. H. A.; Schiavon, M. A.; Pecoraro, E.; Ribeiro, S. J. L.; Ferrari, J. L. $CaTiO_3$:Er^{3+}:Yb^{3+} upconversion from 980 nm to 1550 nm excitation and its potential as cells luminescent probes. *Mater. Chem. Phys.* **2019**, *223*, 391−397.
(33) Vetrone, F.; Boyer, J.-C.; Capobianco, J. A.; Speghini, A.; Bettinelli, M. Significance of Yb^{3+} concentration on the upconversion mechanisms in codoped Y_2O_3:Er^{3+},Yb^{3+} nanocrystals. *J. Appl. Phys.* **2004**, *96*, 661−667.
(34) Auzel, F.; Baldacchini, G.; Laversenne, L.; Boulon, G. Radiation trapping and self-quenching analysis in Yb^{3+}, Er^{3+}, and Ho^{3+} doped Y_2O_3. *Opt. Mater.* **2003**, *24*, 103−109.
(35) Chen, Z.; Gong, W.; Chen, T.; Li, S.; Wang, D.; Wang, Q. Preparation and upconversion luminescence of Er^{3+}/Yb^{3+} codoped $Y_2Ti_2O_7$ nanocrystals. *Mater. Lett.* **2012**, *68*, 137−139.
(36) Hong, G.; Lee, J. C.; Robinson, J. T.; Raaz, U.; Xie, L.; Huang, N. F.; Cooke, J. P.; Dai, H. Multifunctional in vivo vascular imaging using near-infrared II fluorescence. *Nat. Med.* **2012**, *18*, 1841−1846.
(37) Hong, G.; Zou, Y.; Antaris, A. L.; Diao, S.; Wu, D.; Cheng, K.; Zhang, X.; Chen, C.; Liu, B.; He, Y.; Wu, J. Z.; Yuan, J.; Zhang, B.; Tao, Z.; Fukunaga, C.; Dai, H. Ultrafast fluorescence imaging in vivo with conjugated polymer fluorophores in the second near-infrared window. *Nat. Commun.* **2014**, *5*, 4206.
(38) Naczynski, D.; Tan, M.; Zevon, M.; Wall, B.; Kohl, J.; Kulesa, A.; Chen, S.; Roth, C.; Riman, R.; Moghe, P. Rare-earth-doped biological composites as in vivo shortwave infrared reporters. *Nat. Commun.* **2013**, *4*, 1−10.
(39) Nadort, A.; Zhao, J.; Goldys, E. M. Lanthanide upconversion luminescence at the nanoscale: fundamentals and optical properties. *Nanoscale* **2016**, *8*, 13099−13130.
(40) Tan, H.; Xie, S.; Xu, J.; Li, N.; Zhang, C.; Xu, L.; Zheng, J. Branched $NaYF_4$:Yb,Er up-conversion phosphors with luminescent properties for anti-counterfeiting application. *Sci. Adv. Mater.* **2017**, *9*, 2223−2233.
(41) Welsher, K.; Liu, Z.; Sherlock, S. P.; Robinson, J. T.; Chen, Z.; Daranciang, D.; Dai, H. A route to brightly fluorescent carbon nanotubes for near-infrared imaging in mice. *Nat. Nanotechnol.* **2009**, *4*, 773−780.
(42) Perrella, R. V.; Schiavon, M. A.; Pecoraro, E.; Ribeiro, S. J. L.; Ferrari, J. L. Broadened band C-telecom and intense upconversion emission of Er^{3+}/Yb^{3+} co-doped $CaYAlO_4$ luminescent material obtained by an easy route. *J. Lumin.* **2016**, *178*, 226−233.
(43) Yang, Y.; Yang, Z.; Li, P.; Li, X.; Guo, Q.; Chen, B. Dependence of optical properties on the composition in Er^{3+}-doped $xNaPO_3$−(80−x)TeO_2−10ZnO−10Na_2O glasses. *Opt. Mater.* **2009**, *32*, 133−138.
(44) Shao, Q.; Zhang, G.; Ouyang, L.; Hu, Y.; Dong, Y.; Jiang, J. Emission color tuning of core/shell upconversion nanoparticles through modulation of laser power or temperature. *Nanoscale* **2017**, *9*, 12132−12141.
(45) Chen, B.; Liu, Y.; Xiao, Y.; Chen, X.; Li, Y.; Li, M.; Qiao, X.; Fan, X.; Wang, F. Amplifying Excitation-Power Sensitivity of Photon Upconversion in a $NaYbF_4$:Ho Nanostructure for Direct Visualization of Electromagnetic Hotspots. *J. Phys. Chem. Lett.* **2016**, *7*, 4916−4921.
(46) Bednarkiewicz, A.; Wawrzynczyk, D.; Gagor, A.; Kepinski, L.; Kurnatowska, M.; Krajczyk, L.; Nyk, M.; Samoc, M.; Strek, W. Giant enhancement of upconversion in ultra-small Er^{3+}/Yb^{3+}:$NaYF_4$ nanoparticles via laser annealing. *Nanotechnology* **2012**, *23*, 145705.
(47) Berry, M. T.; May, P. S. Disputed mechanism for NIR-to-red upconversion luminescence in $NaYF_4$:Yb^{3+},Er^{3+}. *J. Phys. Chem. A* **2015**, *119*, 9805−9811.
(48) Gregson, D.; Catlow, C. R. A.; Chadwick, A. V.; Lander, G. H.; Cormack, A. N.; Fender, B. E. F. The structure of LaF_3−a single-crystal neutron diffraction study at room temperature. *Acta Crystallogr. Sect. B Struct. Sci.* **1983**, *39*, 687−691.
(49) Evarestov, R. A.; Leko, A. V.; Murin, I. V.; Petrov, A. V.; Veryazov, V. A. Electronic structure of La, O, and LaF, crystals. *Phys. Stat. Solb.* **1992**, *170*, 145.
(50) Persson, K. Materials Data on LaOF (SG:129) by Materials Project. 2014, https://materialsproject.org/materials/mp-7100/ (accessed November 29, 2021).
(51) Modak, B.; Ghosh, S. K. Exploring the role of La codoping beyond charge compensation for enhanced hydrogen evolution by Rh−$SrTiO_3$. *J. Phys. Chem. B* **2015**, *119*, 11089.

https://doi.org/10.1021/acsanm.1c03023
ACS Appl. Nano Mater. 2021, 4, 13562−13572